



Micromagnetic simulations of magnetization reversal in kagome artificial spin ice

Murilo Ferreira Velo , Breno Malvezzi Cecchi ^{*}, and Kleber Roberto Pirota

“Gleb Wataghin” Institute of Physics, University of Campinas, 13083-859 Campinas, São Paulo, Brazil



(Received 20 June 2020; revised 28 November 2020; accepted 1 December 2020; published 17 December 2020)

This work reports micromagnetic simulations used to study magnetization reversal in kagome artificial spin ice, taking into account the actual edge imperfections presented by the magnetic nanoislands as a source of disorder. An important advantage of the micromagnetic approach is to discretize a magnetic element in nanometric domains, allowing access to the sample magnetic moments distribution in detail. The limit case of zero disorder is accessed considering a system composed of perfect magnetic islands. The main result is the prediction of a critical angle between the applied magnetic field and the direction of one of the sublattices, above which Dirac strings emerge. For lower values, the reversal occurs through a bidimensional fashion, being smooth or abrupt depending on whether or not roughness is present, respectively. Finally, our simulations open the question of how the contour imperfections really influence the magnetic response of artificial spin ice.

DOI: [10.1103/PhysRevB.102.224420](https://doi.org/10.1103/PhysRevB.102.224420)

I. INTRODUCTION

Artificial spin ice (ASI) is a magnetic metamaterial composed of ferromagnetic monodomain nanoislands, also called macrospins, arranged in a bidimensional (2D) lattice [1,2]. The kagome configuration [3] is one of the most studied cases because it gives rise to geometrical frustration, although several new arrangements have been considered more recently [1], ranging from brickwork [4] and Shakti [5] to pinwheel [6] and quasiperiodic [7] lattices. Since many of the ASI properties are strongly related to their geometries, they present a considerable variety of interesting phenomena, among which one could mention highly degenerate ground states [2,8], emergent magnetic monopoles (MPs) [3,9], frustration-induced dimensional reduction [3,10], phase transitions [11–13], and programmable spin-wave spectra [14,15]. From the experimental point of view, the fabrication of ASI usually involves lithography techniques to develop the pattern for deposition, with permalloy (Py) the most commonly used magnetic material. Moreover, magnetic microscopy methods, such as photoemission electron microscopy (PEEM) with magnetic contrast [3] or magnetic force microscopy [2,9], are particularly interesting for characterization because they give access to the magnetic orientation of each island of the lattice. Thus, it is possible to construct the hysteresis loop from the images, knowing the magnetic state at each point [3,16,17].

In the early realizations of ASIs, the systems were thermally inactive [18,19], i.e., the macrospins did not exhibit stochastic thermal fluctuations, although such thermal activity has been achieved in more recent samples [20–22]. Thus, several works have addressed field-driven processes in order to induce dynamics [19,23]. For instance, the magnetization reversal of kagome ASI has been experimentally observed to

occur through 1D avalanches of flipped macrospins, referred to as Dirac strings (DSs) [3,9]. This mechanism is usually described by the creation and separation of emergent magnetic MPs of opposite charges, $\pm\Delta Q$, located at the ends of the string. They are calculated based on the so-called dumbbell model [24], where each macrospin of length d is treated as an Ising magnetic moment \mathbf{m} and is replaced by a dumbbell of opposite magnetic charges, $\pm q = \pm m/d$. Each vertex of the lattice has a total charge $Q = \sum_{i=1,2,3} q_i$, which is always an integer multiple of q and where i indexes the three charges that meet at that position. In the initial saturated state, for example, $Q_0 = +q$ or $Q_0 = -q$ depending on whether the vertex has two macrospins pointing into and one out of the vertex (two-in/one-out) or vice versa (one-in/two-out), respectively. These two-in/one-out and one-in/two-out configurations are known as the ice rules, which also dictate the ground state of the kagome lattice in the absence of a magnetic field [3,11]. During the reversal, the total charge of the vertices change from Q_0 to some value Q as the magnetization of the islands flip, so that the MP charge is defined as the charge variation $\Delta Q = Q - Q_0$.

Simulations based on that Ising-like description generally need to assume a switching field distribution of the islands in order to simulate the magnetization reversal [3,9,10,25,26]. Moreover, it is known that this kind of disorder affects several other quasistatic properties of ASI, such as the demagnetization final energy [27], global magnetic coercivity [28], and vertex dynamics induced by a magnetic field [29] or temperature [30]. Commonly, the physical origin of the distribution is attributed to imperfections at the islands surface, remaining from the lithographic process, for example. Indeed, Bryan *et al.* experimentally verified, for Py elongated nanostructures, a coercive field variation of more than 100% as the peak-to-peak edge roughness increased from 27 to 72.5 nm [31]. In that same work, the authors did not verify appreciable roughness on the top surface for samples presenting peak-to-peak edge roughness below 85 nm and, for nominally

^{*}Corresponding author: bmcechi@ifi.unicamp.br

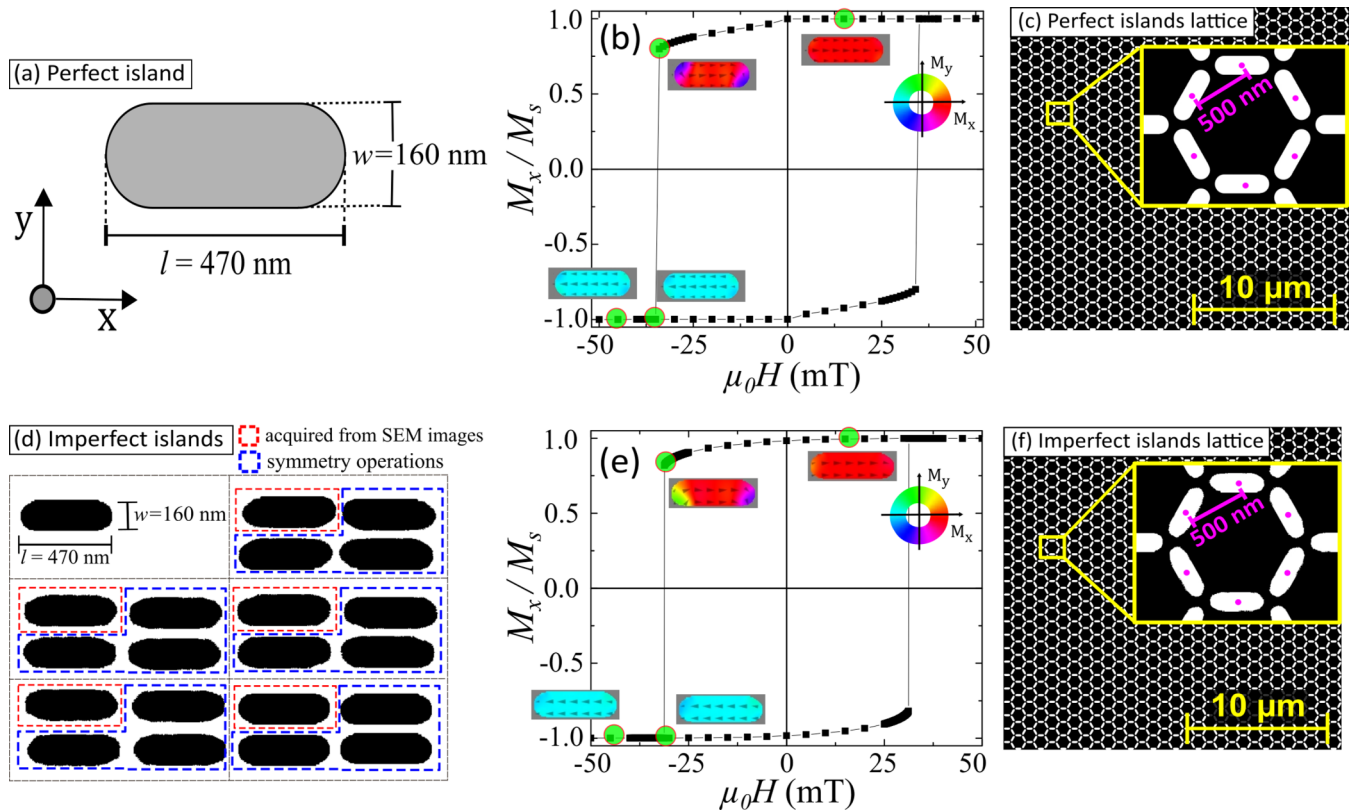


FIG. 1. (a) Single perfect, roughness-free, stadiumlike-shaped island, with length $l = 470$ nm, width $w = 160$ nm, and thickness $t = 20$ nm. (b) Hysteresis curve for an isolated perfect island, where M_x/M_s is the normalized x component M_x of the islands' total magnetization, whose coercive field is $\mu_0 H_c = 34.4$ mT (the field was applied along a direction deviated by 0.001° from the x direction). (c) Simulated kagome array composed of 2536 perfect islands, with lattice parameter 500 nm and total area of $26 \times 24 \mu\text{m}$. (d) The 20 imperfect islands, with different edge roughness, used as building blocks for the imperfect islands lattice. (e) Hysteresis curve of one of the imperfect islands, with coercive field $\mu_0 H_c = 31.2$ mT, which is different from the perfect island's one (field applied along a direction deviated by 0.001° of the x direction). (f) Simulated kagome array composed of 2536 imperfect islands, with lattice parameter of 500 nm and total area of $26 \times 24 \mu\text{m}$.

identical nanostructures, a spread of 20 Oe in coercivity was observed, suggesting the detailed edge shape of roughness could also affect the switching field. Nevertheless, Liou *et al.* verified a more stable magnetic configuration for elongated Py nanostructures with lower aspect ratios (approximately 3:1), evidencing more resistance against edge roughness effects [32]. Nominally identical islands with relatively low aspect ratios are exactly the case of the ASIs considered in this work.

Despite reproducing the magnetic properties mentioned in the last paragraph, Ising-based simulations do not take into account the spatial extent of the islands. Thus, they are not able to model the island's shape and miss the exact magnetization distribution inside them. Moving to a micromagnetic frame, however, both features are naturally embedded, opening the possibility to understand how shape imperfections directly influence those properties. For instance, Kohli *et al.* used micromagnetic simulations (MMSs) to study edge roughness as a source of disorder in a square ASI and concluded that "roughness in the island edges plays a hitherto unrecognized but essential role in the collective behavior of these systems" [28].

Some other works have also addressed further aspects related to the magnetization properties of ASI using MMSs. For

example, field-driven processes in pinwheel arrays [33], the influence of nearest neighbors on the magnetization reversal of a given island [34], and the extent that dimensions of the islands induce chiral MPs whose chirality dictates their directional motion [35] have been studied. However, the main disadvantage of MMSs is that they are more computationally demanding compared to Ising-island simulations. They have been considering only relatively small arrays with dozens of islands at most, so that MMSs of lattices as large as those simulated by Ising-island methods (up to thousands of islands) have not been reported yet [36].

In this work, we report the use of MMSs to study large-size ASIs. The magnetization reversal of a kagome array is simulated, taking into account the intrinsic roughness at the edge of the islands. The main result is the existence of a critical angle θ_c between the applied field and the direction of one of the sublattices, which separates different reversal mechanisms. For angles above θ_c , the reversal happens through 1D avalanches and reproduces the emergence of magnetic MPs and DSs. For angles below θ_c , a different kind of reversal is predicted, which takes place via 2D expansion of the macrospin's domains. Furthermore, the reversal happens more smoothly or abruptly depending on the presence or absence of roughness, respectively.

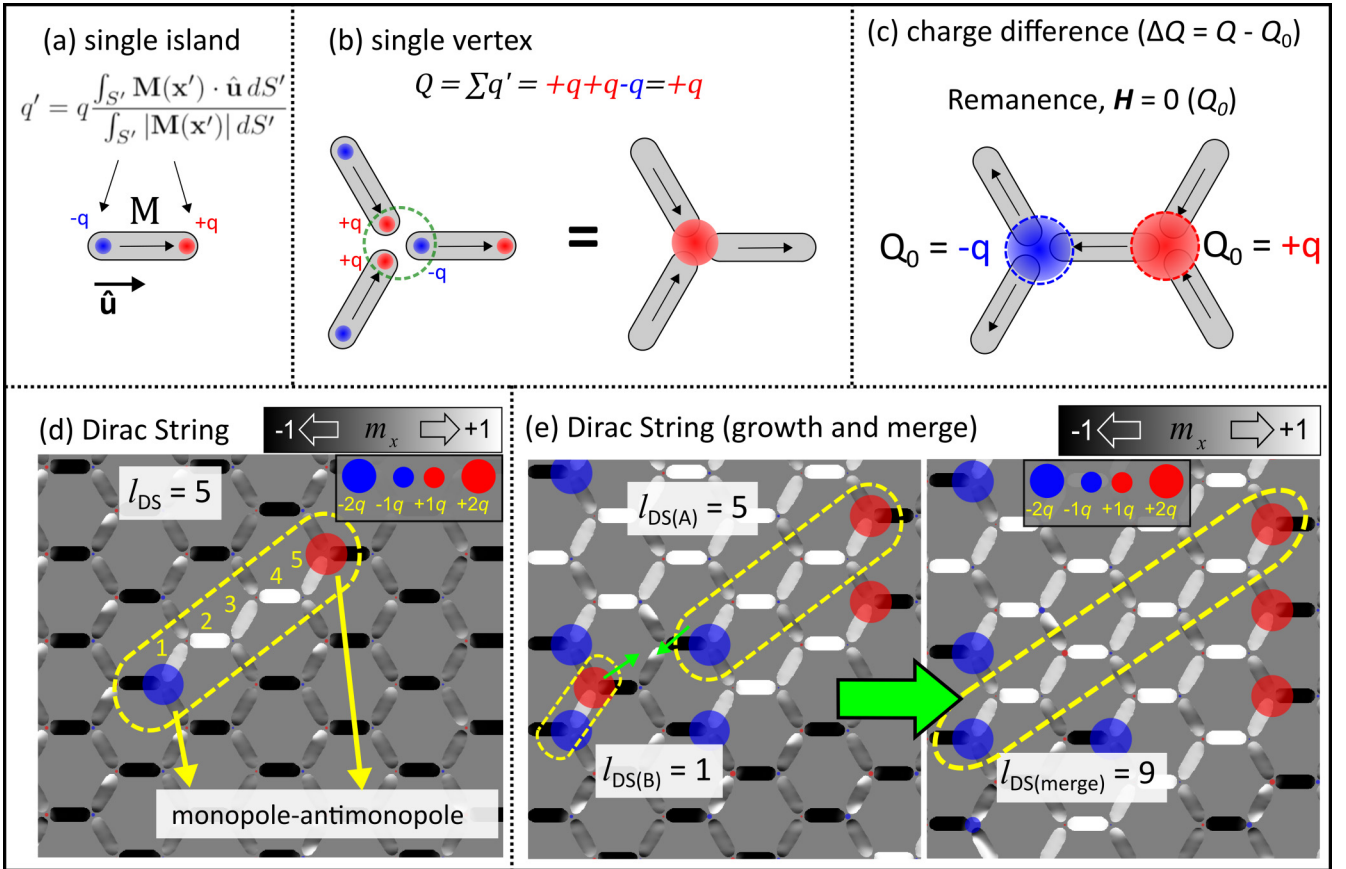


FIG. 2. (a) A single island with uniform magnetization $\mathbf{M} = M_s \hat{\mathbf{u}}$ with two opposite charges $\pm q' = \pm q$ on its ends. (b) A kagome vertex with total charge $Q = +q$. (c) Two neighboring vertices at remanence, with total charges $Q_0 = +q$ and $Q_0 = +q$ (ground-state configuration obeying ice rules). (d) A single Dirac string (DS) with size $l_{DS} = 5$ and its monopole-antimonopole pair (red and blue circles, respectively). (e) Example of two DSs (with $l_{DS(A)} = 5$ and $l_{DS(B)} = 1$) merging to form a new DS with size $l_{DS(merge)} = 9$.

II. MICROMAGNETIC SIMULATIONS

MMSs of the magnetization reversal of ASI were performed using the MUMAX3 open package [37] assisted by an Nvidia GPU Titan X. We simulated a rectangular patch composed of 2536 magnetic islands made of Py, arranged in the kagome lattice with a lattice parameter of 500 nm [insets of Figs. 1(c) and 1(f)]. The simulations were done in a mesh of $6506 \times 6020 \times 1$ cells (maximum mesh memory allocation allowed by the GPU) of sides $l_x = l_y = 4$ nm and $l_z = 20$ nm. These parameters led us to a physical area of $26 \times 24 \mu\text{m}$, which is around 25% of the experimental one ($50 \times 50 \mu\text{m}$) studied by Mengotti *et al.* [3]. As standard micromagnetic Py parameters, we used the saturation magnetization $M_s = 8.0 \times 10^5$ A/m and exchange stiffness $A = 1.3 \times 10^{-11}$ J/m, which leads to an exchange length $l_{\text{exc}} = \sqrt{2A/\mu_0 M_s^2} \approx 5.0$ nm. We notice that $l_z > l_{\text{exc}}$, but because Py has no crystalline anisotropy, the magnetization remains practically restricted to the xy plane and does not vary along the z direction due to the shape anisotropy. The field step was $\mu_0 \Delta H = 5$ mT, while the state was close to saturation and at a maximum of $\mu_0 \Delta H = 1$ mT during the part of the reversal with more activity. Further details can be found in the codes and text available in the Supplemental Material [38].

We considered two different kagome lattices as the objects of study: a perfect, roughness-free lattice and an imperfect lattice composed of islands with roughness on their edge surface. The perfect lattice was built from the replication of one perfect island with a smooth stadiumlike shape, with length $l = 470$ nm, width $w = 160$ nm, and thickness $t = 20$ nm [Figs. 1(a)–1(c)]. As the islands are exactly the same, this arrangement does not exhibit a coercive field distribution.

The imperfect lattice was constructed with islands with similar dimensions, but with roughness on their edges. We acquired the exact contour from the scanning electron microscopy image shown in Ref. [3], using an artificial high-contrast image boundary recognition [Figs. 1(d)–1(f)]. This procedure gave us a set of five different islands, highlighted in red in Fig. 1(d). In order to expand this set, we performed three symmetry operations on each of these five islands: x reflection, y reflection, and x reflection followed by y reflection. These operations are illustrated in detail in the Supplemental Material [38]. The result is a total of 20 distinct elements [Fig. 1(d)]. This new set has a coercive field distribution with mean value $\mu_0 \overline{H_c} = 30.6$ mT and standard deviation $\sigma_c = 0.3$ mT [39]. Finally, for each site of the kagome lattice, we randomly chose one of the 20 imperfect islands to occupy it.

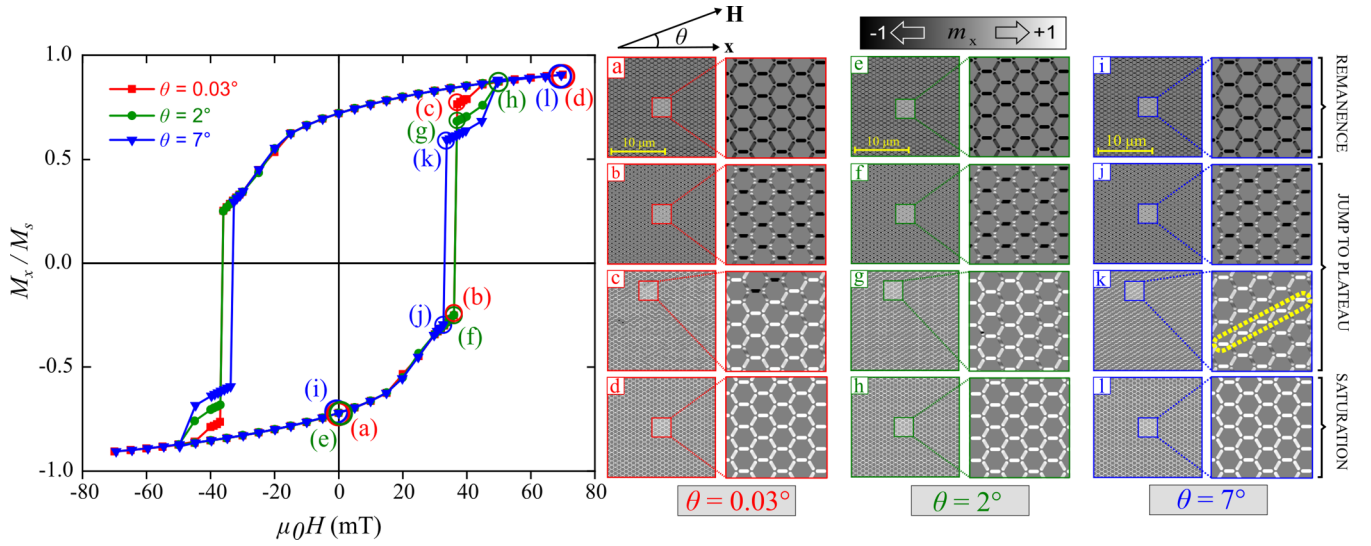


FIG. 3. Left: Hysteresis curves for the perfect identical islands system, where M_x/M_s is the normalized x component M_x of the lattice's total magnetization, for a magnetic field applied with angles $\theta = 0.03^\circ$ (red), $\theta = 2^\circ$ (green), and $\theta = 7^\circ$ (blue) with respect to the x axis. Right: Magnetization states of the system for representative points of the ascending branch of the hysteresis for (a)–(d) $\theta = 0.03^\circ$, (e)–(h) $\theta = 2^\circ$, and (i)–(l) $\theta = 7^\circ$. The gray color map represents the x component m_x of the local reduced magnetization $\mathbf{m}(\mathbf{x}) = \mathbf{M}(\mathbf{x})/M_s$. Note that one of the many Dirac strings is highlighted in yellow in inset (k).

In MMSs, the magnetization of each island is discretized, having internal and detailed distributions, differently from the dumbbell model. Therefore, we generalize the calculation of the “dumbbell” charges, from $\pm q = \pm m/d$ to more accurate values $\pm q'$, in order to account for situations where the averaged island magnetization does not point exactly along its long axis:

$$q' = q \frac{\int_{S'} \mathbf{M}(\mathbf{x}') \cdot \hat{\mathbf{u}} dS'}{\int_{S'} |\mathbf{M}(\mathbf{x}')| dS'}, \quad (1)$$

where $\hat{\mathbf{u}}$ is a unit vector along the island long-axis direction [see Fig. 2(a)], $\mathbf{M}(\mathbf{x}')$ is the island magnetization distribution, and S' is the island surface. Thus, the vertex total charge $Q = \sum_{i=1,2,3} q'_i$ and the MP charge $\Delta Q = Q - Q_0$ are allowed to be noninteger multiples of q . Figures 2(a)–2(c) illustrate the calculation of q' , Q , and ΔQ . It is worth noting that in this work, the charge Q_0 has been calculated in the remanence, i.e., for $H = 0$, because it is when the islands are as similar as possible to Ising macrospins—with uniform magnetization along the long axis—obeying the ice rules [see Fig. 2(c)]. Finally, Figs. 2(d) and 2(e) show a DS and the merging of two minor DSs of lengths $l_{\text{DS(A)}}$ and $l_{\text{DS(B)}}$ into a major DS with length $l_{\text{DS(merge)}} > l_{\text{DS(A)}} + l_{\text{DS(B)}}$, where the DS length is defined as the number of reverted islands connecting a monopole-antimonopole pair.

III. RESULTS AND DISCUSSION

We divided our results into two parts: (i) perfect islands lattice (Sec. III A) and (ii) imperfect islands lattice (Sec. III B). Both results are for an ASI arranged in a kagome lattice, where the difference between them lies in the system building blocks. For case (i), we used identical magnetic islands, with a perfectly smooth geometry (stadium shape). For case (ii), we used islands with roughness, where the building blocks

are not the same (different roughness), which leads to a $\mu_0 H_c$ distribution among the different islands. Finally, we discuss the reversal mechanism by means of the DS nucleation and propagation present in (ii).

A. Perfect islands lattice

We performed simulations of the magnetization reversal process taking the angle θ between the applied magnetic field and the x direction as a parameter. Figure 3 shows the magnetization curves of the perfect islands lattice for angles $\theta = 0.03^\circ$, $\theta = 2^\circ$, and $\theta = 7^\circ$. It is worth noting that the case for $\theta = 0^\circ$ is not reported because the system remains trapped in the initial saturated state, as opposed to an experimental situation where the system is always driven away from the metastability. For $\theta = 0.03^\circ$, the magnetization reversal, as can be seen in Figs. 3(a)–3(d), does not occur by DS creation and propagation, as one could have expected. We first observe a smooth rotation of the magnetization close to the islands' ends [color gradient at the island extremities shown in the insets of Figs. 3(a) and 3(b)]. This is followed by a huge simultaneous magnetization inversion of almost 97% of the islands [white and light-gray islands of Fig. 3(c)], corresponding to a plateau region of the hysteresis. This inversion takes place for $\mu_0 H = 38$ mT, after a single magnetic field step of $\mu_0 \Delta H = 1.0$ mT ($\sim 20\,000$ simulation iterations). Finally, the system approaches the positive saturation by reverting the 3% remaining islands, as shown in Fig. 3(d). For $\theta = 2^\circ$, we notice a similar magnetization reversal, with the absence of DSs [see Figs. 3(e)–3(h)]. The smaller magnetization jump just before the plateau indicates the magnetization reversion of 93% of the islands for approximately the same field value presented in the case of $\theta = 0.03^\circ$. It is followed by the reversion of the 7% remaining islands in a similar fashion as before.

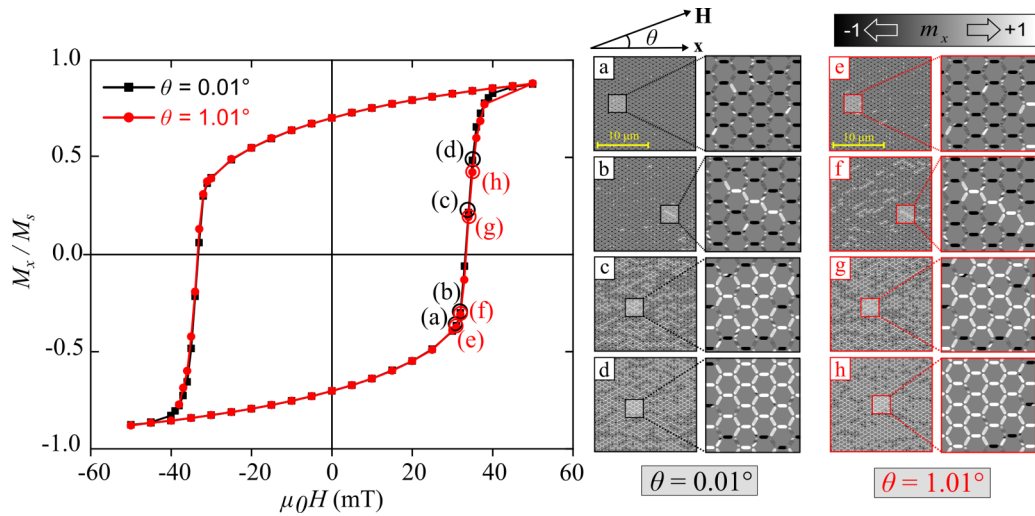


FIG. 4. Left: Hysteresis curves for the imperfect nonidentical islands system, where M_x/M_s is the normalized x component M_x of the lattice's total magnetization, for a magnetic field applied with angles $\theta = 0.01^\circ$ (black) and $\theta = 1.01^\circ$ (red) with respect to the x axis. Right: Magnetization states of the system for representative points of the ascending branch of the hysteresis with (a)–(d) $\theta = 0.01^\circ$ and (e)–(h) $\theta = 1.01^\circ$. The gray color map represents the x component m_x of the local reduced magnetization $\mathbf{m}(\mathbf{x}) = \mathbf{M}(\mathbf{x})/M_s$.

Interestingly, the magnetization reversal occurs through a different mechanism for $\theta = 7^\circ$, as shown in Figs. 3(i)–3(l). The system goes from negative to positive saturation, passing through a highly ordered plateau state, shown in Fig. 3(k), that persists within the field range of $38 < \mu_0 H < 44$ mT. We identified this state to be established by the simultaneous and “infinitely” rapid propagation (within the field step $\mu_0 \Delta H = 1$ mT) of various diagonally oriented DSs extending all over the sample and parallel to each other. One of them is highlighted in yellow in Fig. 3(k). The last minor step, for $\mu_0 H = 44$ mT, forces the overall magnetization to the positive saturation.

Since the perfect islands of this system are physically identical, they all have the same coercive field (namely, $\mu_0 H_c = 34.4$ mT), without distribution, mimicking a disorder-free situation not precisely considered in Ising-island models. As a consequence, the magnetization reversal mechanism evidenced here for perfect identical islands was not previously predicted. The persistence of finitely fast and nonsimultaneous 1D avalanches of DSs was always present, even for systems with a low level of disorder [10].

B. Imperfect islands lattice

The actual case of imperfect, nonidentical islands is of more practical interest because it presents DSs in the magnetic reversal mechanism. Figure 4 shows the results for $\theta = 0.01^\circ$ and $\theta = 1.01^\circ$ and Fig. 5 for $\theta = 7^\circ$. First, for $\theta = 0.01^\circ$ and $\theta = 1.01^\circ$, similar behaviors are observed. The magnetization reversal starts with few islands flipping their magnetization [light-gray islands in Figs. 4(a) and 4(e)], subsequently giving rise to few and sparse elongated DSs, as shown in Figs. 4(b) and 4(f). However, further increase in the applied field leads to a magnetization process mainly dominated by a 2D domain mechanism, as can be seen in Figs. 4(c) and 4(d) for $\theta = 0.01^\circ$ and in Figs. 4(g) and 4(h) for $\theta = 1.01^\circ$. Differently from the perfect islands situation, here the magnetization does not

present a huge jump for low angles. Instead, the reversal happens in a more gradual fashion, evidenced by the hysteresis curve without any pronounced plateau. Note that the few DSs observed are, in this case, just some isolated phenomena, not being observed all over the sample during the entire process. Thus, the reversal mechanism cannot be said to occur by means of DSs.

Despite being taken from similar functional points at respective hysteresis loops (almost the same magnetization and magnetic field value in each small-angle situation), the magnetization snapshots of Fig. 4 reveal different magnetic structures for different θ values. This suggests a highly degenerated macrospin configuration for each functional point of the hysteresis curves for small applied field angles. This behavior is similar to that presented by a thin magnetic film with planar magnetic anisotropy, for an applied magnetic field direction close enough to an easy magnetization axis [40].

Similarly to the perfect islands lattice case, $\theta = 7.0^\circ$ represents an interesting different situation. The reversal is strongly dominated by DS nucleation and propagation, as can be seen in Fig. 5, whereas Fig. 6 shows the hysteresis loop. Increasing the magnetic field from the negative saturation brings the system to remanence at $H = 0$, evidenced in Fig. 5(a). Further increase promotes few islands to flip the magnetization, creating monopole-antimonopole pairs connected by DSs, as can be seen in Fig. 5(b). One can appreciate mainly three phenomena from Figs. 5(c)–5(e) as the reversal proceeds: (i) monopole-antimonopole pair creation, (ii) DS propagation (l_{DS} increases), and (iii) DS merging. Finally, Fig. 5(f) shows the positive saturation state, with the MPs and antimonopoles ordered in the so-called NaCl state, where each nearest neighbor of a MP is an antimonopole, and vice versa [11].

Each MP can be classified according to its mobility [3]. For instance, in the beginning of the reversal, most MPs can move to neighboring vertices by expansion of their associated DSs, so they are called mobile MPs. As the reversal proceeds, a mobile MP eventually hits a DS and can no longer move

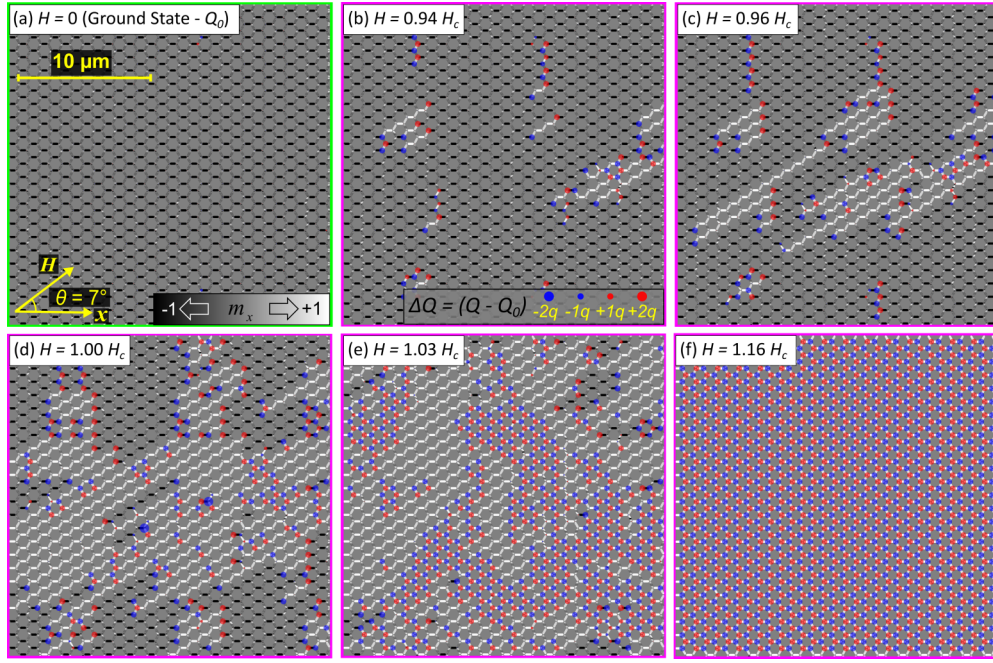


FIG. 5. Simulated monopole-antimonopole pair creation and propagation of Dirac strings for an angle $\theta = 7.0^\circ$ between the magnetic applied field and the x direction. The gray color map represents the x component m_x of the local reduced magnetization $\mathbf{m}(\mathbf{x}) = \mathbf{M}(\mathbf{x})/M_s$. The blue and red dots represent negative and positive monopole magnetic charges $+\Delta Q$ and $-\Delta Q$, respectively (having possible noninteger $\Delta Q/q$ values). The ground state (a) is used to calculate the initial reference charge Q_0 for the monopole charge distribution $\Delta Q = Q - Q_0$, where $-2q \leq \Delta Q \leq +2q$. The snapshots correspond to the points highlighted in Fig. 6: $H = 0$ highlighted in green, and $H = 0.94H_c$, $H = 0.96H_c$, $H = 1.00H_c$, $H = 1.03H_c$, and $H = 1.16H_c$ highlighted in purple, where $\mu_0 H_c (= 27.3 \text{ mT})$ refers to the coercive field of the lattice.

because all macrospins of that vertex have already flipped. When this happens, the mobile MP becomes a trapped MP. This information is made quantitative in Fig. 6, which shows the fractions v_m and v_t of the mobile and trapped MPs, respectively, as a function of the applied field. v_m is high (close to one) until $H = H_c$, where H_c is the coercive field of the lattice,

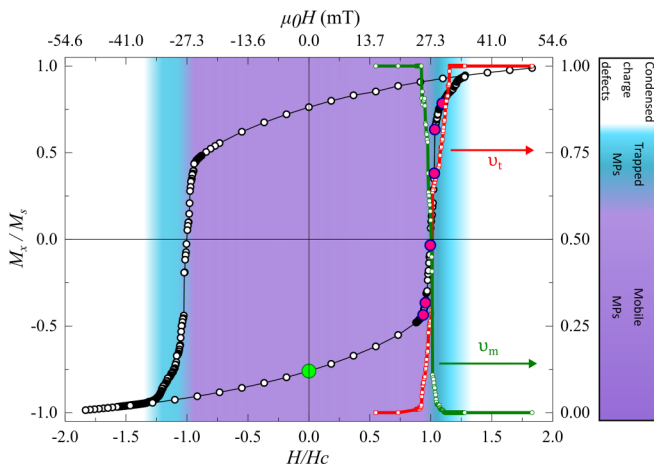


FIG. 6. The hysteresis curve (black) of the imperfect islands system for a magnetic field applied with angle $\theta = 7^\circ$ with respect to the x direction, where M_x/M_s is the normalized x component M_x of the lattice's total magnetization. The fraction v_m of mobile monopoles (green) and the fraction v_t of trapped monopoles (red). The green circle is the remanence state shown in Fig. 5(a) and the purple circles are the states shown in Figs. 5(b)–5(f).

because most MPs are mobile in the beginning. For $H > H_c$, some MPs begin to hit DSs, so v_t grows and v_m falls. The final stage corresponds to the system achieving positive saturation, where $v_t = 1$ and $v_m = 0$, by flipping the last remaining islands. At this point, it is said that the MPs condense because they occupy all vertices in the positive saturation (NaCl state).

The MP mobility is linked with the DS phenomena since the reversal mechanism occurs by means of DS nucleation, growth, and merging, with the DS expansion due to the mobile MPs at the DS free ends. The DSs are observed, as shown in Fig. 5, by direct observation of the snapshots. However, their change in the MP mobility is probed by the MP fractions (green and red curves in Fig. 6). Then, as in the experimental counterpart of this system, we observe a magnetic system restricted to 2D space, which reverts its magnetization by 1D structures, identified as the DS emergence.

We note that the emergence of MPs and DSs in this simulation is directly determined by the roughness of the islands since this is the only modification from the previous case of perfect identical islands. However, the experimental hysteresis curve reported by Mengotti *et al.*, constructed from PEEM images, just smooths the plateau that appeared in the perfect island case, whereas in our simulation the plateau is completely suppressed. In addition, other features presented by the experimental curves of v_m and v_t are also absent in ours, such as a plateau of v_m in the beginning of the reversal and a slower growth to the saturation value $v_m = 1$ [3].

These deviations can be associated to four main issues. First, border effects, whose presence can play an important role in the magnetostatic behavior of coupled nanomag-

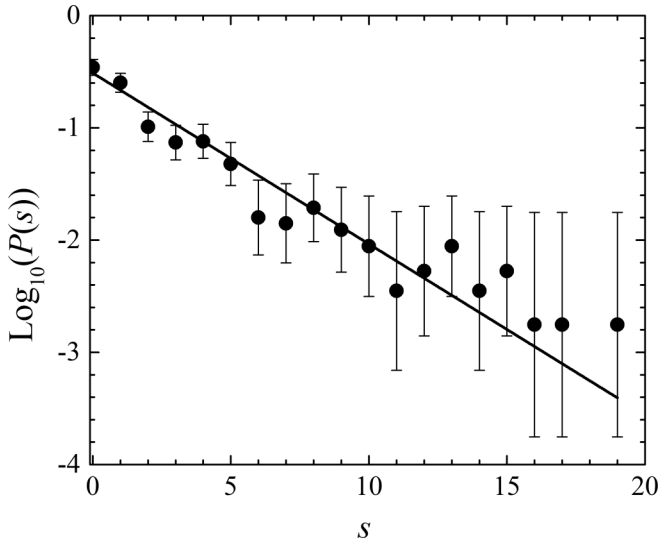


FIG. 7. Probability distribution $P(s)$ that a Dirac string will have its length increased by $\Delta l = s$ within a field step $\mu_0 H = 0.1$ mT during the magnetization reversal of the imperfect islands lattice. The data were taken from all field steps between $H = 0.9H_c$ and $H = 1.04H_c$ of the ascending branch of the hysteresis shown in Fig. 6. The error bar of a point $P(s_0)$ was calculated as $1/\sqrt{N(s_0)}$, where $N(s_0)$ is the frequency of avalanches with size s_0 .

nets [41], are less significant in the experimental results than in our simulations. This is because the experimental sample has a total area of $50 \times 50 \mu\text{m}$, which is approximately four times larger than our simulated lattice, of which just a minor central region was considered for the construction of the curves. Second, the experimental PEEM images do not resolve the magnetization within the islands as detailed as MMSs. Third, the curves measured by Mengotti *et al.* were obtained with the sample at remanence, i.e., after turning off the field at each point. And fourth, we considered just a limited set of 20 distinct islands to construct the whole imperfect islands lattice.

It is also interesting to look at the dimensional nature of the magnetization reversal. The snapshots of Fig. 5 visually suggest that it proceeds in a 1D fashion, as a result of the nucleation and propagation of DS. In a broader context, the inversion of spins belonging to a finite region of a magnetic material is known as an avalanche [42,43]. The probability distribution $P(s)$ of finding an avalanche of size s can indicate the dimension of the reversal mechanism. Namely, it obeys a power law for 2D and 3D systems [42,43] and an exponential law for 1D systems [3,10,44]. Figure 7 shows the probability $P(s)$ of a DS to increase its length by $\Delta l = s$ within a field step of $\mu_0 \Delta H = 0.1$ mT, calculated from all field steps between $H = 0.9H_c$ and $H = 1.04H_c$ of the ascending branch of the hysteresis of Fig. 6. It can be seen that $P(s)$ decays exponentially, in agreement with the reported experimental result [3], confirming the 1D fashion of the reversal. This feature is referred to as dimensional reduction since the dimension of the reversal mechanism (1D) is smaller than the dimension of the system where it takes place (2D) [3,10]. It is an interesting property because typical magnetization reversals occur by growth of domains that have the same dimension of

the material (2D in thin films and 3D in bulk materials, for example).

C. Critical angle

We notice that the direction of the DS propagation, for both perfect [Fig. 3(k)] and imperfect (Fig. 5) islands, primarily follows the upward diagonal direction of the applied field. In order to certify that, we simulated the symmetrical configuration, $\theta = -7^\circ$, and the strings appeared in the downward diagonal direction for both systems. In fact, this diagonal preference is also exhibited by experimental samples [3], which was later argued as an indication of some angle offset between the applied field and the long axis of the horizontal islands [35]. The presence of an offset angle is also a requisite for suitable reproduction by Ising-island models [3,10].

In addition, our results indicate that there is a critical angle θ_c below which DSs do not occur. In other words, not only is an offset angle θ between the applied field and the x axis needed for DSs to appear in a kagome ASI, but θ must be larger than θ_c .

The existence of a critical angle can be better understood by comparing our results with standard features of mixed anisotropic thin films. Our kagome ASI could be compared with a structured film with mixed uniaxial magnetic anisotropies, configured by two easy magnetization directions separated by an angle of $\beta = 60^\circ$. In this comparison, the two preferred magnetization axes are characterized by the island's long directions. When such systems are subjected to an applied magnetic field, the magnetization lies along one of the easy axes, as long as the angle between the field and the axis is kept sufficiently small. But, when the angle is increased, it reaches a critical value at which the magnetization abruptly jumps to the other easy axis, reproducing a spin-flopping-like process [45].

Thus, it is reasonable to expect similar features in a kagome ASI. In fact, a closer inspection of the plateau states of the perfect islands system at the low-angle regime reveals that these states gradually change, with less islands flipping simultaneously as θ increases [see Figs. 3(c) for $\theta = 0.03^\circ$ and 3(g) for $\theta = 2^\circ$, for example].

The fact that our MMSs reproduce a more realistic 3D characteristic of elementary magnetic islands allows us to observe phenomena that are impossible to be reproduced in models which consider each island to be a rigid two-level magnetic moment. Such geometric characteristics cause the magnetic islands to present thin-film features for certain applied field conditions. As an illustration, let us take the case of magnetization reversal of our ASI for a magnetic field direction almost parallel to the x direction. Under these conditions, the inversion of the islands' magnetization takes place in an irreversible and noncoherent way (as shown in Figs. 3 and 4 for perfect and imperfect systems), exactly reproducing the magnetization process presented by a thin magnetic film under the same applied magnetic field conditions (nucleation and propagation of magnetic domains, propagation of domain walls, etc.), i.e., an applied magnetic field direction parallel to an easy magnetization axis, as already discussed above.

Therefore, it is natural to expect that in the case of a kagome ASI, when increasing the angle of application of the

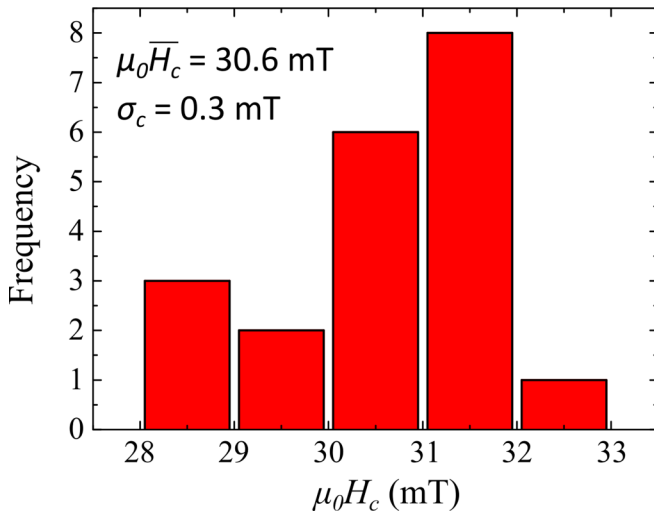


FIG. 8. Coercive field distribution of the 20 islands with edge roughness used to construct the imperfect islands lattice. It has a mean value of $\mu_0 \overline{H_c} = 30.6$ mT and standard deviation of $\sigma_c = 0.3$ mT.

magnetic field in relation to the x direction, we will find a critical value for which the magnetization process abruptly jumps to the imposed direction; in this case, not by the intrinsic magnetic anisotropy of the islands, but by that of the kagome lattice geometry. In our case, for an applied magnetic field direction angle that is greater than $\theta = 7^\circ$, the inversion of macrospins occurs preferably confined in the direction defined by diagonal islands. The magnetization process direction abruptly changes to a critical field, exactly reproducing the described biaxial thin-film situation.

D. Coercive field distribution

In the MMSs of the imperfect islands lattice, an island's coercive field distribution naturally comes along by simply taking into account the more realistic description of the island's shape, which includes small edge roughness. By simulating the individual hysteresis of each of the 20 imperfect islands used to construct the lattice, with the applied field slightly deviated from the long axis by $\theta = 0.001^\circ$ for the same reasons explained in Sec. III A, we found the distribution of coercive fields shown in Fig. 8. It has a mean value of $\mu_0 \overline{H_c} = 30.6$ mT and standard deviation of $\sigma_c = 0.3$ mT, leading to a ratio $\sigma_c / \mu_0 \overline{H_c} \approx 0.01$.

In reported Ising-island models, each island of the lattice has a switching field H_s , defined as the value of the projection of the local magnetic field along the island long axis above which the island flips its magnetization. The distribution of H_s is an input of the simulation, usually chosen to be Gaussian, with adjustable standard deviation σ_s . The value of σ_s is phenomenologically estimated to be the one that better fits the experimental hysteresis and MP mobility curves. Previous works have found this value to be $\sigma_s / \mu_0 \overline{H_s} \approx 0.13$ [3,10].

Although H_c and H_s are, strictly speaking, different physical quantities, it is expected that they have at least the same order of magnitude. We see, however, that $\sigma_c / \mu_0 \overline{H_c} \approx 0.01$ is one order of magnitude below $\sigma_s / \mu_0 \overline{H_s} \approx 0.13$. Therefore, roughness with sizes suggested by Refs. [3,10] is not capable alone of explaining such degree of H_s dispersion. Recognizing that these morphological imperfections are probably the main source for an H_c (and H_s) distribution, this result opens the question of whether the phenomenological σ_s value determined from Ising-island simulations really has a physical meaning.

Furthermore, our distribution does not resemble a Gaussian one. This might be associated with the small number of 20 islands—of which only 5 were truly independent—that were sampled to obtain the distribution. However, it could also indicate that an H_s Gaussian distribution hypothesis may not be reasonable. It is known that arrays of interacting magnetic nanostructures can have a log-normal switching field distribution, for example [46]. In any case, it would be interesting to know the shape of all the islands of an experimental sample so that this question could be properly resolved.

IV. CONCLUSIONS

MMSs were used to study interesting and important aspects of quasistatic magnetization reversal in a kagome ASI. We conclude that the magnetization reversal mechanism strongly depends on the angle θ between the external applied field with respect to the direction of one of the sublattices and on the edge roughness of real magnetic elements. The critical angle θ_c determines the dimensionality of the reversal, which is 2D if $\theta < \theta_c$ or 1D if $\theta > \theta_c$. The presence or lack of roughness indicates whether the process will be more smooth or abrupt, respectively. This result suggests the existence of a phaselike diagram of the reversal mechanism, taking into account the mentioned parameters. Detailed simulations are being performed with fine variation of those parameters and will be presented in a future work. Finally, we observe that the dispersion of the islands' coercive field distribution of our simulation is one order of magnitude below that estimated by the indirect phenomenological approach of reported Ising-island simulations. This opens the question of whether the latter corresponds to the real physical situation, which reinforces the importance of employing MMSs to investigate quasistatic phenomena in ASIs at the expense of Ising-like simulations.

ACKNOWLEDGMENTS

This research was financially supported by the Brazilian funding agencies Conselho Nacional de Desenvolvimento e Científico e Tecnológico (CNPq), Coordenação de Aperfeiçoamento de Pessoal de Nível Superior (CAPES), and Fundação de Amparo à Pesquisa do Estado de São Paulo (FAPESP—Grants No. 2017/10581-1 and No. 2019/23317-6).

M.F.V. and B.M.C. contributed equally to this work.

[1] S. H. Skjærvø, C. H. Marrows, R. L. Stamps, and L. J. Heyderman, Advances in artificial spin ice, *Nat. Rev. Phys.* **2**, 13 (2020).

[2] R. F. Wang, C. Nisoli, R. S. Freitas, J. Li, W. McConville, B. J. Cooley, M. S. Lund, N. Samarth, C. Leighton, V. H. Crespi, and P. Schiffer, Artificial “spin ice” in a geometrically frustrated

- lattice of nanoscale ferromagnetic islands, *Nature (London)* **439**, 303 (2006).
- [3] E. Mengotti, L. J. Heyderman, A. F. Rodríguez, F. Nolting, R. V. Hügli, and H.-B. Braun, Real-space observation of emergent magnetic monopoles and associated Dirac strings in artificial kagome spin ice, *Nat. Phys.* **7**, 68 (2011).
 - [4] J. Li, X. Ke, S. Zhang, D. Garand, C. Nisoli, P. Lammert, V. H. Crespi, and P. Schiffer, Comparing artificial frustrated magnets by tuning the symmetry of nanoscale permalloy arrays, *Phys. Rev. B* **81**, 092406 (2010).
 - [5] I. Gilbert, G.-W. Chern, S. Zhang, L. O'Brien, B. Fore, C. Nisoli, and P. Schiffer, Emergent ice rule and magnetic charge screening from vertex frustration in artificial spin ice, *Nat. Phys.* **10**, 670 (2014).
 - [6] R. Macêdo, G. M. Macauley, F. S. Nascimento, and R. L. Stamps, Apparent ferromagnetism in the pinwheel artificial spin ice, *Phys. Rev. B* **98**, 014437 (2018).
 - [7] B. Farmer, V. S. Bhat, A. Balk, E. Teipel, N. Smith, J. Unguris, D. J. Keavney, J. T. Hastings, and L. E. De Long, Direct imaging of coexisting ordered and frustrated sublattices in artificial ferromagnetic quasicrystals, *Phys. Rev. B* **93**, 134428 (2016).
 - [8] C. Nisoli, R. Wang, J. Li, W. F. McConville, P. E. Lammert, P. Schiffer, and V. H. Crespi, Ground State Lost but Degeneracy Found: The Effective Thermodynamics of Artificial Spin Ice, *Phys. Rev. Lett.* **98**, 217203 (2007).
 - [9] S. Ladak, D. E. Read, G. K. Perkins, L. F. Cohen, and W. R. Branford, Direct observation of magnetic monopole defects in an artificial spin-ice system, *Nat. Phys.* **6**, 359 (2010).
 - [10] R. V. Hügli, G. Duff, B. O'Conchuir, E. Mengotti, A. F. Rodríguez, F. Nolting, L. J. Heyderman, and H. B. Braun, Artificial kagome spin ice: Dimensional reduction, avalanche control and emergent magnetic monopoles, *Philos. Trans. R. Soc. A* **370**, 5767 (2012).
 - [11] G. Möller and R. Moessner, Magnetic multipole analysis of kagome and artificial spin-ice dipolar arrays, *Phys. Rev. B* **80**, 140409 (2009).
 - [12] L. Anghinolfi, H. Luetkens, J. Perron, M. G. Flokstra, O. Sendetskyi, A. Suter, T. Prokscha, P. M. Derlet, S. L. Lee, and L. J. Heyderman, Thermodynamic phase transitions in a frustrated magnetic metamaterial, *Nat. Commun.* **6**, 8278 (2015).
 - [13] O. Sendetskyi, V. Scagnoli, N. Leo, L. Anghinolfi, A. Alberca, J. Lüning, U. Staub, P. M. Derlet, and L. J. Heyderman, Continuous magnetic phase transition in artificial square ice, *Phys. Rev. B* **99**, 214430 (2019).
 - [14] S. Lendinez and M. B. Jungfleisch, Magnetization dynamics in artificial spin ice, *J. Phys.: Condens. Matter* **32**, 13001 (2019).
 - [15] S. Gliga, E. Iacocca, and O. G. Heinonen, Dynamics of reconfigurable artificial spin ice: Toward magnonic functional materials, *APL Mater.* **8**, 40911 (2020).
 - [16] Y. Li, G. W. Paterson, G. M. Macauley, F. S. Nascimento, C. Ferguson, S. A. Morley, M. C. Rosamond, E. H. Linfield, D. A. MacLaren, R. Macêdo, C. H. Marrows, S. McVitie, and R. L. Stamps, Superferromagnetism and domain-wall topologies in artificial "pinwheel" spin ice, *ACS Nano* **13**, 2213 (2019).
 - [17] T. S. de Paiva, J. H. Rodrigues, L. A. S. Mól, A. R. Pereira, J. Borne, P. P. Freitas, and C. I. L. de Araujo, Effects of magnetic monopoles charge on the cracking reversal processes in artificial square ices, *Sci. Rep.* **10**, 9959 (2020).
 - [18] G. Möller and R. Moessner, Artificial Square Ice and Related Dipolar Nanoarrays, *Phys. Rev. Lett.* **96**, 237202 (2006).
 - [19] C. Nisoli, R. Moessner, and P. Schiffer, Colloquium: Artificial spin ice: Designing and imaging magnetic frustration, *Rev. Mod. Phys.* **85**, 1473 (2013).
 - [20] A. Farhan, P. M. Derlet, A. Kleibert, A. Balan, R. V. Chopdekar, M. Wyss, L. Anghinolfi, F. Nolting, and L. J. Heyderman, Exploring hyper-cubic energy landscapes in thermally active finite artificial spin-ice systems, *Nat. Phys.* **9**, 375 (2013).
 - [21] J. Drisko, S. Daunheimer, and J. Cumings, FePd₃ as a material for studying thermally active artificial spin ice systems, *Phys. Rev. B* **91**, 224406 (2015).
 - [22] H. Stopfel, E. Östman, I.-A. Chioar, D. Greving, U. B. Arnalds, T. P. A. Hase, A. Stein, B. Hjörvarsson, and V. Kapaklis, Magnetic order and energy-scale hierarchy in artificial spin-ice structures, *Phys. Rev. B* **98**, 014435 (2018).
 - [23] L. J. Heyderman and R. L. Stamps, Artificial ferroic systems: Novel functionality from structure, interactions and dynamics, *J. Phys.: Condens. Matter* **25**, 1 (2013).
 - [24] C. Castelnovo, R. Moessner, and S. L. Sondhi, Magnetic monopoles in spin ice, *Nature (London)* **451**, 42 (2008).
 - [25] P. Mellado, O. Petrova, Y. Shen, and O. Tchernyshyov, Dynamics of Magnetic Charges in Artificial Spin Ice, *Phys. Rev. Lett.* **105**, 187206 (2010).
 - [26] Y. Shen, O. Petrova, P. Mellado, S. Daunheimer, J. Cumings, and O. Tchernyshyov, Dynamics of artificial spin ice: A continuous honeycomb network, *New J. Phys.* **14**, 35022 (2012).
 - [27] Z. Budrikis, P. Politi, and R. L. Stamps, Diversity Enabling Equilibration: Disorder and the Ground State in Artificial Spin Ice, *Phys. Rev. Lett.* **107**, 217204 (2011).
 - [28] K. K. Kohli, A. L. Balk, J. Li, S. Zhang, I. Gilbert, P. E. Lammert, V. H. Crespi, P. Schiffer, and N. Samarth, Magneto-optical Kerr effect studies of square artificial spin ice, *Phys. Rev. B* **84**, 180412(R) (2011).
 - [29] Z. Budrikis, P. Politi, and R. L. Stamps, Disorder regimes and equivalence of disorder types in artificial spin ice, *J. Appl. Phys.* **111**, 07E109 (2012).
 - [30] Z. Budrikis, K. L. Livesey, J. P. Morgan, J. Akerman, A. Stein, S. Langridge, C. H. Marrows, and R. L. Stamps, Domain dynamics and fluctuations in artificial square ice at finite temperatures, *New J. Phys.* **14**, 35014 (2012).
 - [31] M. T. Bryan, D. Atkinson, and R. P. Cowburn, Experimental study of the influence of edge roughness on magnetization switching in Permalloy nanostructures, *Appl. Phys. Lett.* **85**, 3510 (2004).
 - [32] S. H. Liou, R. F. Sabirianov, S. S. Jaswal, J. C. Wu, and Y. D. Yao, Magnetic domain patterns of rectangular and elliptic arrays of small permalloy elements, *J. Magn. Magn. Mater.* **226-230**, 1270 (2001).
 - [33] G. W. Paterson, G. M. Macauley, Y. Li, R. Macêdo, C. Ferguson, S. A. Morley, M. C. Rosamond, E. H. Linfield, C. H. Marrows, R. L. Stamps, and S. McVitie, Heisenberg pseudo-exchange and emergent anisotropies in field-driven pinwheel artificial spin ice, *Phys. Rev. B* **100**, 174410 (2019).
 - [34] I. Panagiotopoulos, Magnetostatic bias in Kagome artificial spin ice systems, *Phys. B: Condens. Matter* **486**, 21 (2016).
 - [35] N. Rougemaille, F. Montaigne, B. Canals, M. Hehn, H. Riahi, D. Lacour, and J.-C. Toussaint, Chiral nature of magnetic

- monopoles in artificial spin ice, *New J. Phys.* **15**, 35026 (2013).
- [36] J. Leliaert, M. Dvornik, J. Mulkers, J. De Clercq, M. V. Milosevic, and B. Van Waeyenberge, Fast micromagnetic simulations on GPU-recent advances made with MUMAX(3), *J. Phys. D* **51**, 123002 (2018).
- [37] A. Vansteenkiste, J. Leliaert, M. Dvornik, M. Helsen, F. Garcia-Sanchez, and B. Van Waeyenberge, The design and verification of MUMAX3, *AIP Adv.* **4**, 153 (2014).
- [38] See Supplemental Material at <http://link.aps.org/supplemental/10.1103/PhysRevB.102.224420> for access to the MUMAX codes and details about the symmetry operations performed upon the initial set of five imperfect islands.
- [39] The coercive field distribution, presented in Sec. III D, was calculated considering the hysteresis curve for each isolated imperfect island, with the magnetic field $\mu_0 \mathbf{H}$ applied along a direction deviated by a small angle of 0.001° from the x direction.
- [40] B. D. Cullity and C. D. Graham, in *Introduction to Magnetic Materials* (Wiley, Boboken, New Jersey, 2008), Chap. 11.
- [41] C.-I. Dobrotă and A. Stancu, Tracking the individual magnetic wires' switchings in ferromagnetic nanowire arrays using the first-order reversal curves (FORC) diagram method, *Phys. B: Condens. Matter* **457**, 280 (2015).
- [42] J. P. Sethna, K. A. Dahmen, and C. R. Myers, Crackling noise, *Nature (London)* **410**, 242 (2001).
- [43] J. P. Sethna, K. A. Dahmen, and O. Perkovic, Random-field Ising models of hysteresis, [arXiv:cond-mat/0406320](https://arxiv.org/abs/cond-mat/0406320).
- [44] O. A. Chubykalo, J. M. González, and J. González, Avalanches as propagating domain walls in a micromagnetic model, *Physica D* **113**, 382 (1998).
- [45] B. D. Cullity and C. D. Graham, in *Introduction to Magnetic Materials* (Wiley, Boboken, New Jersey, 2008), Chap. 7.
- [46] T. Thomson, G. Hu, and B. D. Terris, Intrinsic Distribution of Magnetic Anisotropy in Thin Films Probed by Patterned Nanostructures, *Phys. Rev. Lett.* **96**, 257204 (2006).